Journal of Magnetic Resonance 308 (2019) 106586

Contents lists available at ScienceDirect

Journal of Magnetic Resonance

journal homepage: www.elsevier.com/locate/jmr

Frequency-chirped dynamic nuclear polarization with magic angle spinning using a frequency-agile gyrotron

Chukun Gao [a,b,1], Nicholas Alaniva [a,b,1], Edward P. Saliba [a,b], Erika L. Sesti [a], Patrick T. Judge [a,c], Faith J. Scott [a], Thomas Halbritter [d], Snorri Th. Sigurdsson [d], Alexander B. Barnes [a,b,*]

[a] Department of Chemistry, Washington University in St. Louis, St. Louis, MO 63130, USA
[b] Physical Chemistry, ETH-Zurich, Vladimir-Prelog-Weg 2, 8093 Zurich, Switzerland
[c] Department of Biochemistry, Biophysics & Structural Biology, Washington University in St. Louis, St. Louis, MO 63110, USA
[d] University of Iceland, Department of Chemistry, Science Institute, Dunhaga 3, 107 Reykjavik, Iceland

ARTICLE INFO

Article history:
Received 28 June 2019
Revised 15 August 2019
Accepted 28 August 2019
Available online 29 August 2019

Keywords:
Dynamic nuclear polarization
Nuclear magnetic resonance
Magic angle spinning
Frequency-chirped DNP
Frequency-agile gyrotron
Frequency-chirped microwaves

ABSTRACT

We demonstrate that frequency-chirped dynamic nuclear polarization (DNP) with magic angle spinning (MAS) improves the enhancement of nuclear magnetic resonance (NMR) signal beyond that of continuous-wave (CW) DNP. Using a custom, frequency-agile gyrotron we implemented frequency-chirped DNP using the TEMTriPol-1 biradical, with MAS NMR at 7 T. Frequency-chirped microwaves yielded a DNP enhancement of 137, an increase of 19% compared to 115 recorded with CW. The chirps were 120 MHz-wide and centered over the trityl resonance, with 7 W microwave power incident on the sample (estimated 0.4 MHz electron spin Rabi frequency). We describe in detail the design and fabrication of the frequency-agile gyrotron used for frequency-chirped MAS DNP. Improvements to the interaction cavity and internal mode converter yielded efficient microwave generation and mode conversion, achieving >10 W output power over a 335 MHz bandwidth with >110 W peak power. Frequency-chirped DNP with MAS is expected to have a significant impact on the future of magnetic resonance.

1. Introduction

In dynamic nuclear polarization (DNP), the large polarization present in an electron spin reservoir is transferred to nuclear spins, thereby enhancing the intrinsically low sensitivity of nuclear magnetic resonance (NMR) [1–13]. Solid-state NMR and DNP can be combined with magic angle spinning (MAS), which averages anisotropic interactions by rotating the sample about an axis set at 54.7° with respect to the static magnetic field. MAS NMR is a spectroscopic platform that can describe complex molecular and biological architectures [14–20]. Continuous-wave (CW) DNP enhances NMR signal-to-noise by orders of magnitude at moderate magnetic fields and cryogenic sample temperatures. DNP performance is expected to improve at higher magnetic field strengths (14–28 T) and higher temperatures with time-domain DNP [21–24].

Time-domain DNP holds considerable promise to extend MAS DNP to room temperature, at which high-resolution spectra of dynamic molecules can be recorded. MAS DNP experiments are typically performed at cryogenic temperatures (<100 K) due to spin relaxation properties competing with DNP mechanisms. In order to improve performance at high fields and room temperature with time-domain DNP and MAS, a microwave source of sufficient power is required to control electron spins with pulses [21]. Between time-domain DNP and CW DNP lies frequency-chirped DNP, which improves upon CW DNP with modulations in the frequency of the microwave irradiation. Important contributions from Han, Ansermet, Bodenhausen, and colleagues have clearly demonstrated the advantages of modulated, or chirped DNP in static experiments [25–27]. We emphasize that the experiments described in this contribution are not referred to as "time-domain" DNP, as time-domain DNP should be reserved to describe well-characterized coherent electron spin manipulation. Here we describe a variation of the microwave frequency in the time domain, which can be referred to as chirped DNP, or chirped microwaves and its application with MAS.

Gyrotron oscillators are coherent microwave sources well-suited for chirped and time-domain DNP since they can be made frequency-agile, output relatively high power levels, and efficiently scale to higher frequencies [26,28–36]. Current MAS instrumentation prohibits the implementation of a microwave resonator, which is often used in static experiments to generate a high

* Corresponding author at: Department of Chemistry, Washington University in St. Louis, St. Louis, MO 63130, USA.
E-mail address: abarnes@ethz.ch (A.B. Barnes).
[1] These authors contributed equally.

https://doi.org/10.1016/j.jmr.2019.106586
1090-7807/

electron Rabi frequency [37,38]. However, with relatively high power output, gyrotrons do not require a sample resonator to achieve the necessary microwave fields for time-domain DNP, thereby enabling frequency-chirped and time-domain DNP with MAS.

Here, we present frequency-chirped DNP with MAS using a coherent, high-power frequency-agile gyrotron. We achieve a 19% gain in enhancement over CW DNP with frequency chirps of 7 W microwave power incident on a sample, which is spun at 4.5 kHz at a temperature of 87 K and a magnetic field of 7 T. The power output of the custom-built 198 GHz frequency-agile gyrotron exceeds 100 W, with a bandwidth of 335 MHz. We describe in detail the design and assembly of this frequency-agile gyrotron used for frequency-chirped DNP in rotating solids. The development of high-power, frequency-agile gyrotrons is expected to drive time-domain MAS DNP toward room temperature and high magnetic fields.

2. Methods and results

2.1. Frequency-chirped MAS DNP

The spectra in Fig. 1A show a 19% increase in cross effect DNP enhancement using frequency-chirped microwaves compared to CW irradiation, on a sample of 4 M [U-^{15}N, ^{13}C] urea doped with 5 mM TEMTriPol-1 [39,40]. Microwave frequency chirps over the trityl resonance of TEMTriPol-1 (Fig. 2B) were performed using a frequency-agile gyrotron according to the pulse sequence shown in Fig. 1B. An arbitrary waveform generator (AWG) was used to create voltage waveforms for frequency chirps, which were then amplified 1000× by a high-voltage amplifier (TREK, Inc., Lockport, NY). The amplifier output was electrically connected to the gyrotron anode to control the potential and achieve frequency agility, in the form of frequency-chirped waveforms. The voltage output from the AWG and the high-voltage amplifier are shown in Fig. 2A. Frequency chirps covered a range of 120 MHz and were centered at 197.670 GHz (Fig. 2B). The time for one microwave chirp was 78 μs, with 50 μs up and 28 μs down in frequency. These chirps were repeated over a 20 s DNP period (τ_{pol}, Fig. 1B). The range of the chirps is illustrated by a polychromatic block superimposed on a simulated EPR spectrum of a 1:1 trityl/TEMPO combination. The EPR simulation was generated with a spin-physics package written in our laboratory, and does not account for interactions between electron spins.

Frequency-chirped microwaves over the resonance condition of the radical have been implemented previously to improve NMR sensitivity through electron decoupling [41,42]. Here, chirped

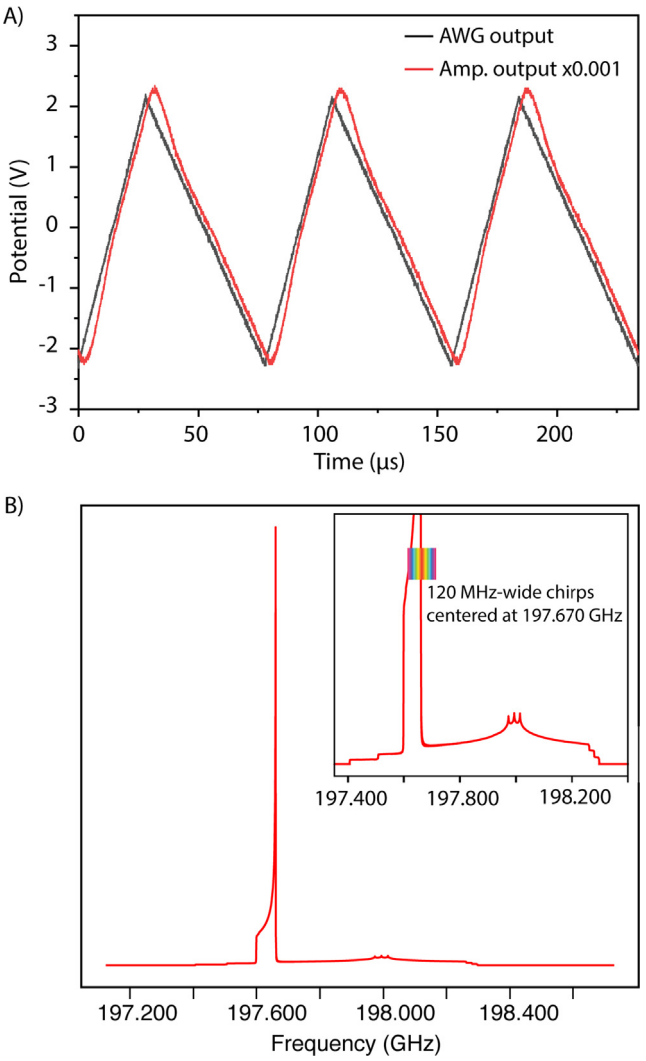

Fig. 2. (A) The voltage waveforms used for frequency-chirped DNP. The black trace is the output of the AWG and the red trace is the high-voltage amplifier output, scaled down by a factor of 1000. (B) Simulated EPR spectrum of 1:1 trityl/TEMPO combination. Both the continuous wave irradiation and frequency chirps are centered at 197.670 GHz, the condition for maximum positive cross effect enhancement [43]. The expansion on the upper-right depicts the range and location of the frequency chirps (polychromatic block) with respect to the EPR spectrum. (For interpretation of the references to colour in this figure legend, the reader is referred to the web version of this article.)

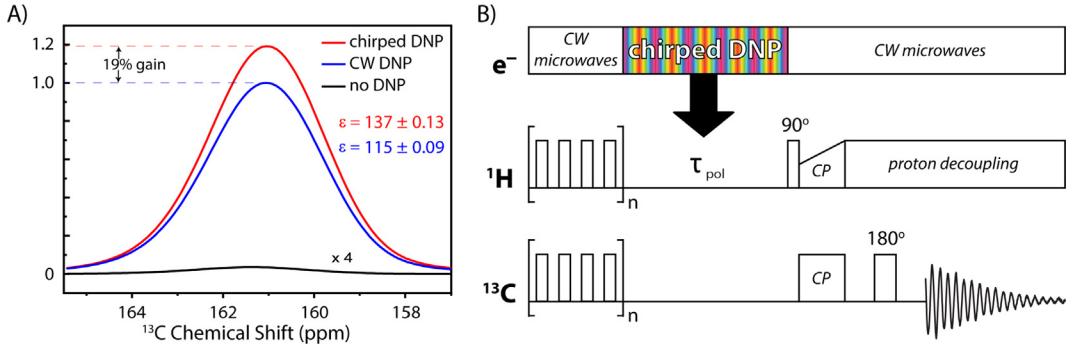

Fig. 1. (A) Spectra of 4 M [U-^{15}N, ^{13}C] urea with 5 mM TEMTriPol-1 in d_8-glycerol, D_2O, and H_2O (60%/30%/10% by volume). The black line is NMR signal without microwave irradiation. The blue line is a CW DNP-enhanced spectrum with an enhancement of 115. The red line is a DNP-enhanced spectrum using frequency chirps with an enhancement of 137. (B) The DNP cross-polarization (CP)-MAS sequence with frequency chirps (polychromatic block) used to conduct frequency-chirped DNP. See Section 2.2 for further experimental details. (For interpretation of the references to colour in this figure legend, the reader is referred to the web version of this article.)

microwaves are applied over the maximum positive cross-effect enhancement condition during the DNP period to increase the DNP enhancements. The DNP period of 20 s utilizes polarization transfer through proton spin diffusion.

2.2. Experimental details for frequency-chirped MAS DNP

The frequency-chirped DNP experiments were performed using a custom-built DNP MAS NMR spectrometer. The spectrometer features two unique elements: a frequency-agile gyrotron and a four-channel, cryogenic transmission-line probe, both of which were designed and assembled at Washington University in St. Louis. A Redstone spectrometer console (Tecmag, Inc., Houston, TX) was used in conjunction with TomCo radiofrequency (RF) amplifiers (TomCo, Adelaide, Australia) to provide RF pulses to the transmission line probe for NMR experiments. The AWG used to generate the voltage waveforms was housed in the Redstone spectrometer as an integrated channel.

Experiments were performed in a 7.1584 T magnetic field with ^{1}H and ^{13}C Larmor frequencies of 300.1790 MHz and 75.4937 MHz, respectively. The sequence employed ^{1}H–^{13}C cross-polarization MAS (CP-MAS) with a rotor-synchronized Hahn echo (Fig. 1B). A 20 s ($1.26*T_{1DNP}$) DNP transfer period was used during the experiments (Fig. 1B), based on the 15 s DNP buildup time. To remove magnetization buildup, a series of saturation pulses were applied to both the ^{1}H and the ^{13}C spins before the DNP period. CW microwaves of 197.670 GHz irradiated the sample during the saturation, CP, spin-echo, and signal acquisition periods (Fig. 1B). The ^{13}C γB_1 was 33 kHz, and the ^{1}H γB_1 was ramped over the Hartmann-Hahn matching condition to conduct efficient CP. The ^{1}H γB_1 was 83 kHz for the excitation pulse and two pulse phase modulation (TPPM) decoupling [44].

The sample, 4 M [U-^{13}C, ^{15}N] urea with 5 mM TEMTriPol-1 in a cryoprotecting matrix of d_8-glycerol, D_2O, and H_2O (60%/30%/10% by volume), was spun at 4.5 kHz at 87 K for all experiments (a <1 K increase in sample temperature is observed with microwaves on the sample, as determined with KBr T_1 measurements [45]). The temperature was monitored by a calibrated temperature sensor. The TEMTriPol-1 biradical contains a Finland trityl and a 4-amino-TEMPO tethered through a glycine linker. 4-amino-TEMPO is a nitroxide monoradical with a broad electron paramagnetic resonance (EPR) lineshape (~900 MHz), whereas Finland trityl is a stable organic monoradical with a relatively narrow EPR lineshape (~60 MHz). With an EPR profile (Fig. 2B) width that exceeds the ^{1}H Larmor frequency, TEMTriPol-1 utilizes the cross effect DNP mechanism. The microwaves from frequency-agile gyrotron were attenuated to provide an incident power of 7 W and an estimated electron Rabi frequency of 0.4 MHz on the sample. 7 W was used as the optimized power to yield the highest DNP enhancement. The microwave power was attenuated with an adjustable copper-slit apparatus that allowed a variable amount of microwave power to pass to the sample. Incident microwave power was calculated using water-load power measurements and previously-determined attenuation of the reduced-diameter waveguide that interfaces with the NMR MAS probe head. The beam current was maintained at 183 mA, varying by less than 3 mA during microwave chirping. The gyrotron operating parameters are summarized in Table 1.

2.3. Gyrotron power output

The gyrotron achieved a peak power of 112 W, and a frequency bandwidth of 335 MHz with power >10 W (Fig. 3). The microwave power was measured with a calorimeter (Scientech, Inc., Boulder, CO), which was calibrated at multiple operation parameters using a water load. The frequency was detected with a frequency measurement system (Bridge 12 Technologies, Inc., Framingham, MA). All experiments were conducted with a beam current of 183 mA. The gyrotron achieved an output efficiency of 4.4% with 112 W power output at 14 kV beam potential (V_b) and 183 mA beam current (I_b).

Table 1
Gyrotron operating parameters.

Operating mode $TE_{m,n,q}$	$TE_{5,2,q}$
Frequency	197.570–197.905 GHz
Voltage tuning range	335 MHz
Cavity magnetic field B	7.16 T
Cyclotron harmonic	1st
Beam voltage V_b	9–14 kV
Beam current I_b	183 mA
Output power	up to 112 W
Compression factor	29

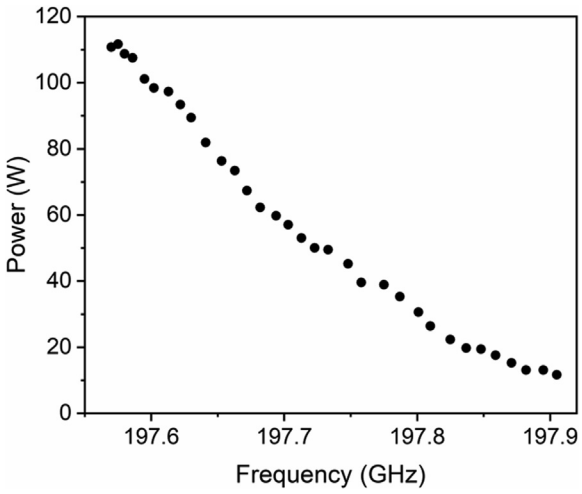

Fig. 3. Power and bandwidth of the 198 GHz gyrotron. The microwave power shown was measured at the gyrotron window. A power output of >10 W is available over 335 MHz bandwidth, with a peak power of 112 W.

We note that the commercially available 263 GHz CW gyrotrons manufactured by CPI (Communications & Power Industry) for Bruker Biospin DNP spectrometers, operating at TE_{03} mode, can output 75 W microwave power at slightly higher efficiency (~10%) with a 15 kV and 50 mA electron beam [36,46]. However, the microwave tuning range in this comparable commercial gyrotron is 100 MHz and there is currently no capability for fast frequency modulation.

3. Gyrotron design and construction

3.1. Improvements in gyrotron design

In a gyrotron, electrons are thermionically emitted from a barium-impregnated tungsten ring when the cathode is heated by an alternating current. A potential between the cathode and anode accelerates the electron beam, whose radius is compressed as it propagates through the magnetic field. The electron beam reaches a maximum compression in the interaction cavity, where a combination of electron cyclotron motion and phase bunching converts kinetic energy into microwave energy. This gyrotron generates microwaves in the $TE_{5,2,q}$ mode. Acceleration of electron beam partially determines the electron cyclotron frequency, and therefore the frequency of the microwaves generated. The spent electron beam exits the cavity and propagates to the water-cooled copper collector. Microwaves propagate through the internal mode converter where they are converted to a Gaussian-like

mode before being directed out of the gyrotron tube through a sapphire window.

This gyrotron utilizes a ceramic break (Fig. 4) to electrically isolate the anode such that the potential can be controlled by high-voltage waveforms to achieve microwave frequency agility. We have used previous gyrotrons to develop novel techniques such as electron decoupling [41–43]. Here we describe the design and construction of a gyrotron with improved power output for frequency-chirped DNP. Major design improvements were made in three main areas: the magnetron injection gun (MIG), the interaction cavity, and the internal mode converter (Fig. 4).

3.1.1. Magnetron injection gun (MIG)

The MIG provides a reservoir of electrons and the necessary geometry for electron beam generation. Fig. 5 illustrates the MIG design of a gyrotron described by Scott et al. (will be referred to as "Scott et al. gyrotron"), which utilized an in-body water cooling system to maintain ambient operating temperature for the MIG [43]. The proximity of the brass connection to the grounded gyrotron magnet bore resulted in several arcing events when the potential was modulated for frequency chirps. In the improved design these brass connections were removed and external air cooling was used instead, maximizing the space between the MIG and the magnet bore to avoid arcing events.

3.1.2. Interaction cavity

The alignment of the cylindrical interaction cavity and the precision of its radius are paramount for obtaining high-power microwave output at the intended frequency and mode. Tapered sections on either side of the interaction cavity prevent undesired microwave modes (parasitic oscillations) (Fig. 7). To facilitate precise fabrication of the interaction cavity, this gyrotron design features an interaction cavity body separate from the tapered segments. The interaction cavity was attached to the up-taper using set screws with pins to ensure proper alignment. While the Scott et al. gyrotron featured a 30 mm-long interaction cavity (Fig. 7B and red box of cross section in Fig. 4B), this gyrotron was designed with a cavity length of 25 mm (Figs. 6 and 7A and the red box of cross section in Fig. 4A) [43]. Note, the 25 mm length is roughly 17 wavelengths (198 GHz), and is sufficient to lead to the excitation of hybridized axial modes in the cavity and continuous frequency tuning, as has been observed previously [31,47].

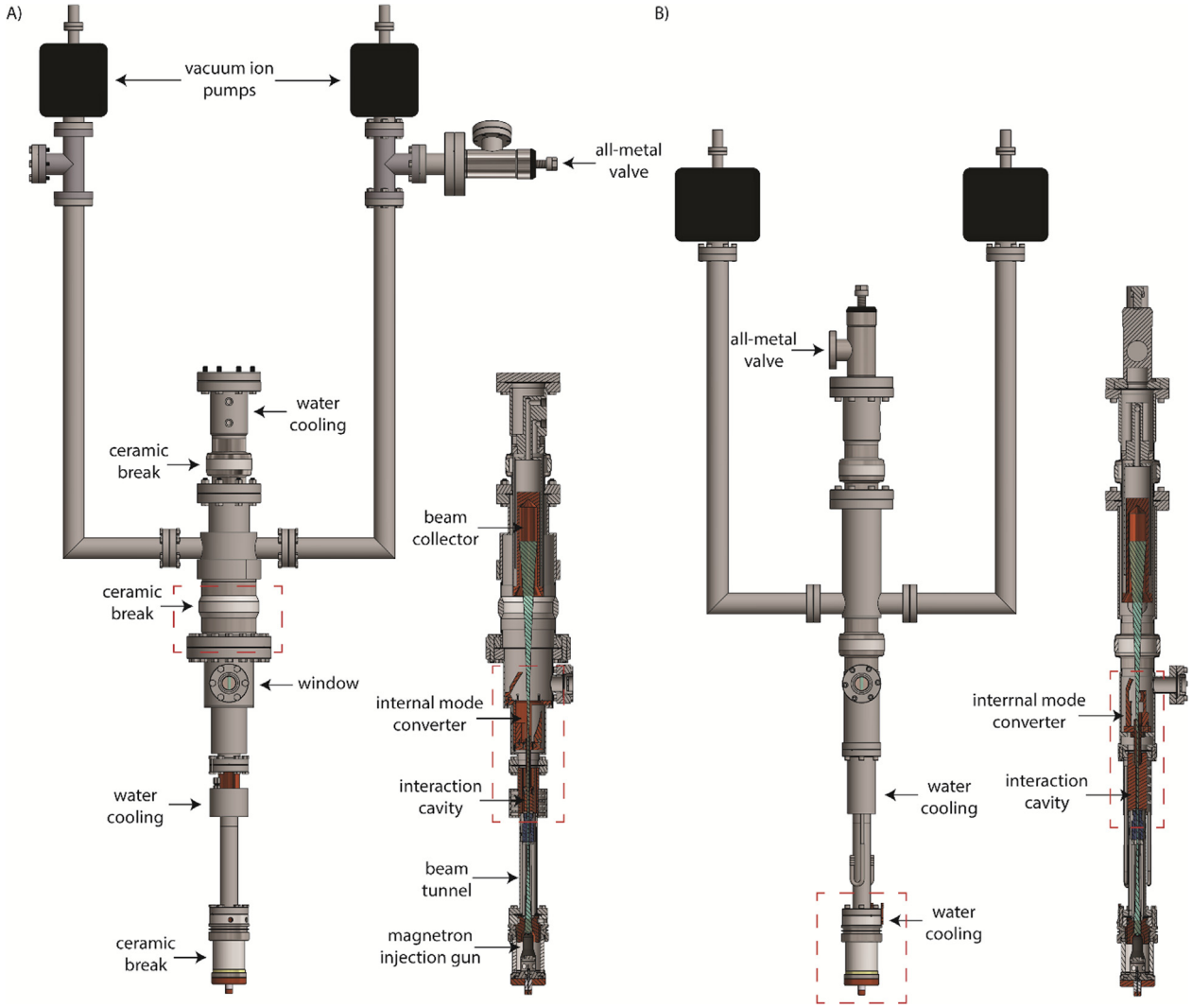

Fig. 4. Schematics of frequency-agile gyrotrons. (A) Full view and cross section of the improved gyrotron for frequency-chirped DNP experiments. (B) Full view and cross section of the gyrotron described by Scott et al. [43]. Red dashed boxes indicate areas that are shown in later figures with detail. (For interpretation of the references to colour in this figure legend, the reader is referred to the web version of this article.)

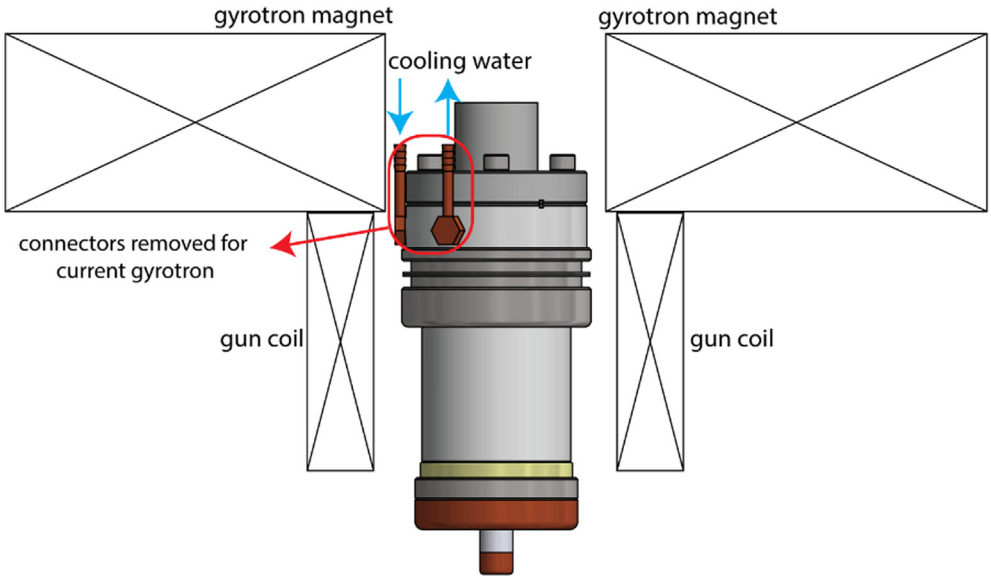

Fig. 5. Schematic of the MIG with brass connectors to water cooling lines in Scott et al. gyrotron [43]. These connectors were removed in the current gyrotron.

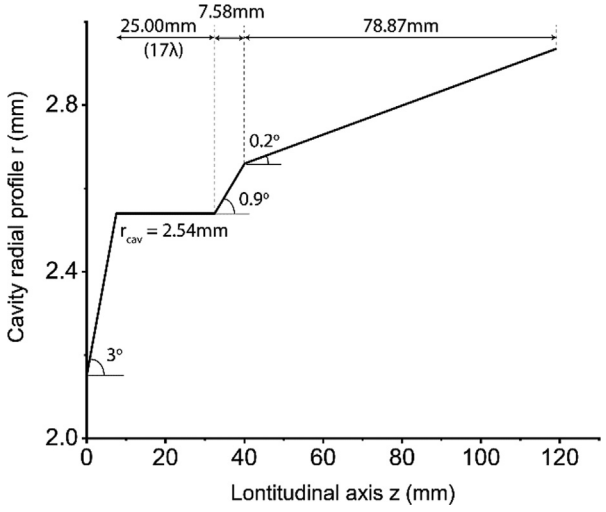

Fig. 6. Geometry of the interaction cavity and up-taper in the current 198 GHz gyrotron. The interaction cavity contains a down-taper and a 25 mm straight section. The 86 mm up-taper is machined as a separate piece.

3.1.3. Internal mode converter

The $TE_{5,2,q}$ mode microwaves generated in the interaction cavity travel up and are directed toward a series of parabolic mirrors by the helical cut of the Vlasov launcher (Fig. 7A and B). The $TE_{5,2,q}$ is a rotating mode, so the Vlasov launcher needs to be helically cut to optimize mode conversion (Fig. 8B). The series of concave mirrors continue to shape the microwave beam profile until the microwaves are directed out of gyrotron through the sapphire window [43,47]. The resulting microwave beam with Gaussian-like mode couples efficiently to the $HE_{1,1}$ mode supported by the corrugated, overmoded waveguide [48].

Microwave power is lost when reflected by mirrors with slight misalignment, so reducing the number of mirrors reduces the possibility of misalignment and increases power output. The current gyrotron uses two concave mirrors rather than three described previously by Scott et al. (Figs. 7A and 8) [43]. The orientation and location of the mirrors were optimized for microwave mode conversion, with stainless steel dowel pins for proper alignment. Mirror surface geometry and alignment were optimized by Bridge12 Technologies, Inc. (Framingham, MA) using an electromagnetics simulation program (Fig. 8C). The supporting structures were then designed in Autodesk Inventor (Autodesk Inc., San Rafael, CA) to align the mirrors and properly direct microwaves out of the gyrotron window. Copper mirrors were fabricated on a computer numerical control milling machine by Ramco Machine (Rowley, MA).

Since microwaves are not directed out of the window with 100% efficiency, stray microwaves are absorbed by the gyrotron body. The temperature of the ceramic break above the window (Fig. 9 and red box of full view in Fig. 4A) rises as the ceramic break region absorbs microwaves improperly reflected by the internal mode converter. This can be an effect of misaligned mirrors and/or the generation of non-$TE_{5,2,q}$ mode microwaves. The improvements made to interaction cavity and internal mode converter led to more efficient microwave generation and $TE_{5,2,q}$-Gaussian mode conversion, which contribute to the maximum microwave power output of 112 W.

3.1.4. Design improvements for future gyrotrons

The current gyrotron experienced a microleak at the welding joint of the ceramic break and flange assembly above the window (Fig. 9 and red box of full view in Fig. 4A). The microleak occurred due to the different stainless steel thickness and uneven heat conductance around the welding joints. The vacuum pressure inside the gyrotron body with the microleak was in the order of 10^{-6} Torr with a turbomolecular pump (Edward T-Station 75, Bolten, UK). After fixing the leak, the vacuum pressure reduced to 10^{-8} Torr. To prevent this issue in the future, the connecting part (yellow in Fig. 9B and C) between the ceramic break and flange will be extended to match the stainless steel thickness on both sides of the welding joint.

3.2. Gyrotron construction

Gyrotron construction requires purchasing of commercial parts as well as incorporating them with custom-designed and custom-built parts. Most gyrotron parts were machined in the Washington University Chemistry Department machine shop, with welding conducted at Laciny Bros., Inc. (University City, MO). The brazing

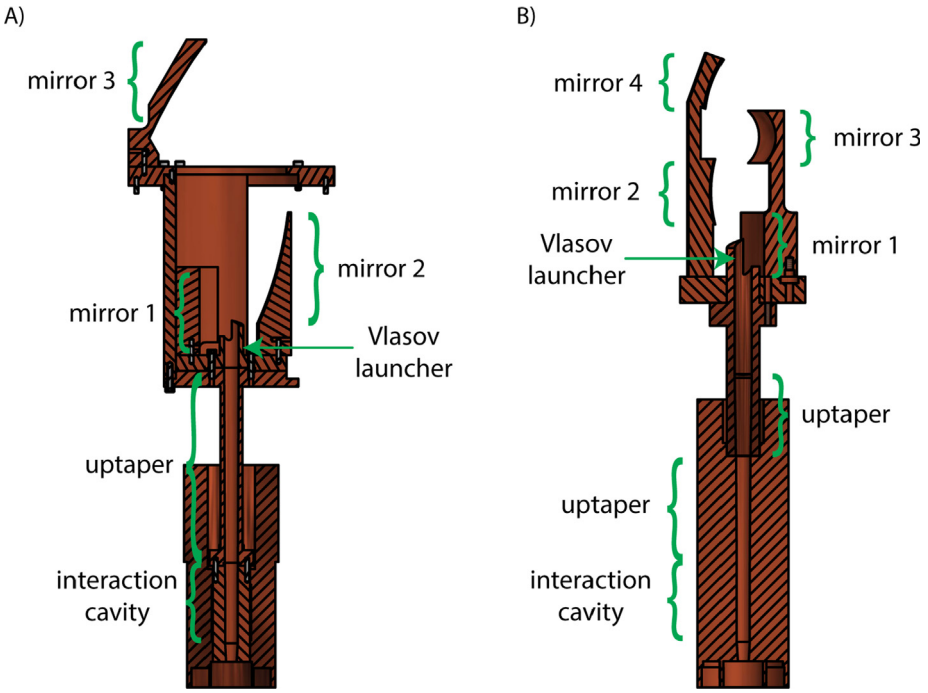

Fig. 7. Section views of internal mode converter and interaction cavity assembly of (A) the current gyrotron and (B) the Scott et al. gyrotron [43].

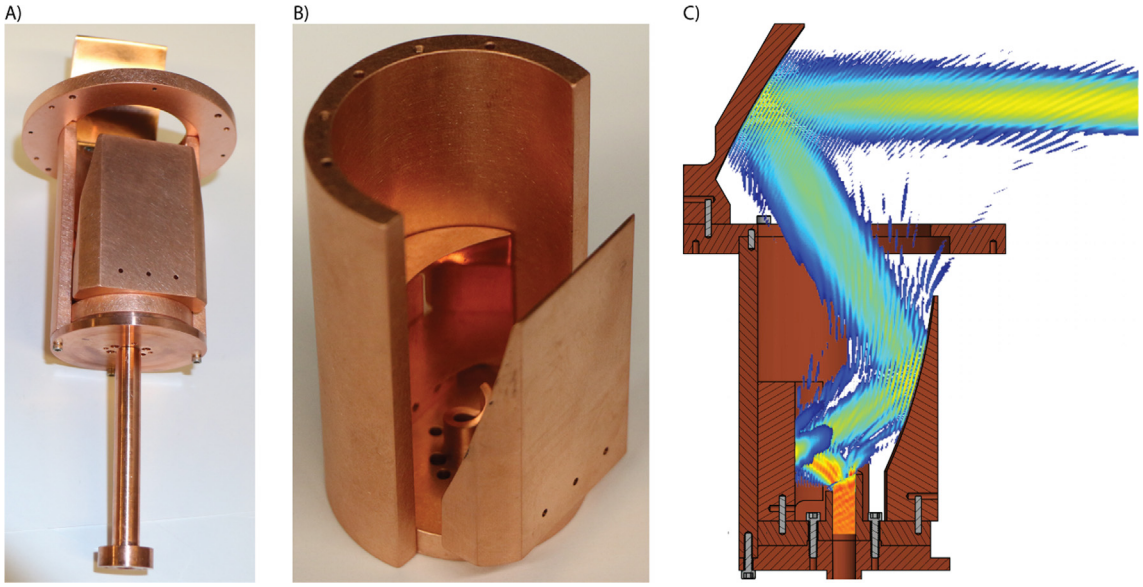

Fig. 8. Internal mode converter of the current gyrotron. (A) Photograph of the internal mode converter assembly. (B) Photograph of the lower two mirrors and the helical Vlasov launcher. (C) Section view of microwave intensity simulation in the internal mode converter. Microwave intensity plots were calculated by Bridge 12 Technologies, Inc.

required for stainless steel and copper connection was done by Ceramic-To-Metal Seals, Inc. (Winchester, MA). Ceramic breaks and CF flanges were provided by MDC Vacuum Products LLC. (Hayward, CA). Vacuum ion pumps were purchased from Duniway Stockroom Corp. (Fremont, CA). The 7 T cryogen-free gyrotron magnet was custom developed by Cryomagnetics, Inc. (Oak Ridge, TN) and is used, in conjunction with the gyrotron, to generate microwave irradiation for all DNP experiments. The superconducting gyrotron magnet has an inner bore diameter of 83.8 mm. The cavity is positioned at the magnet center, where the magnetic field is 7.16 T. The emitter is located 238 mm lower than the cavity, where the superconducting magnetic field is 3.36 T. A smaller, resistive "gun coil" magnet is installed below the superconducting magnet (at the MIG, Fig. 5) for fine adjustment of the gyrotron operation.

An ultra-high vacuum ($\leq 10^{-8}$ Torr) inside the gyrotron is imperative for optimal performance. Oxygen and water molecules can react with the cathode emitter at high temperatures, resulting in an increased work function and sub-optimal electron emission. Also, remaining gas present between cathode and anode, which are under high potential during operation, could become ionized and cause arcing. These important aspects of gyrotron operation require careful attention in construction to achieve the ultra-high vacuum.

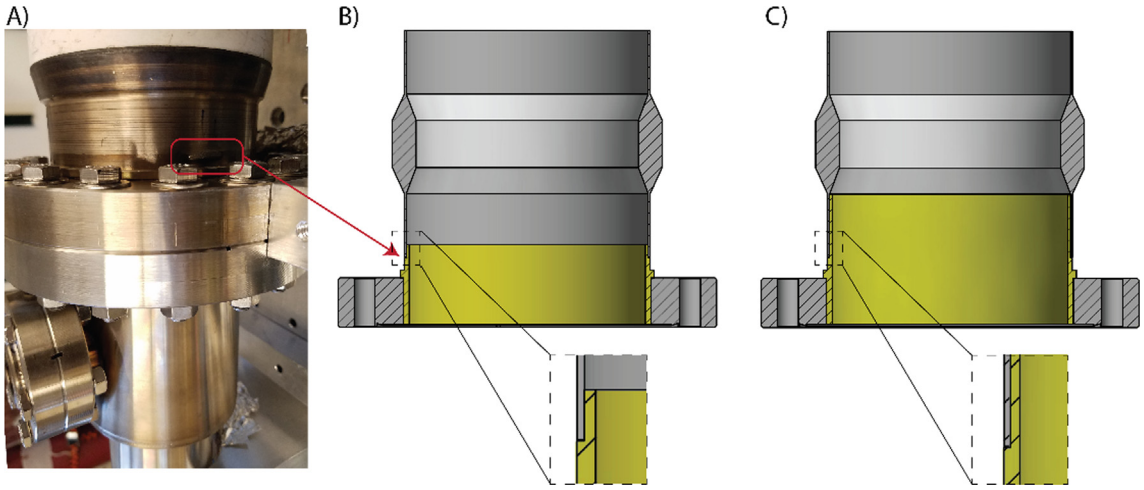

Fig. 9. Ceramic break and flange assembly. (A) Photograph of the welding on the assembly. The re-welding to fix the microleak is indicated in the red box. (B) Schematic of the assembly that had a microleak at the welding joint. The connecting part between ceramic break and flange is indicated in yellow. (C) Schematic of the improved connection between ceramic break and flange for future designs to avoid microleaks. (For interpretation of the references to colour in this figure legend, the reader is referred to the web version of this article.)

3.2.1. Cleaning

A water-based detergent was first used to remove visible greases from machining, followed by acetone to remove detergent and water from stainless-steel surfaces. Ethanol was then used to remove remaining acetone and water due to its higher volatility. Copper parts, such as the internal mode converter and interaction cavity, were cleaned by sonication in ethanol for 30 min because of their delicate features and geometry. Lint-free wipes were used during cleaning to avoid fibers on the inner surface of gyrotron parts.

3.2.2. Leak check and assembly

After cleaning, a helium leak detector (Pfeiffer Vacuum, Nashua, NH) was used to examine all welding joints on each gyrotron part, as well as flange connections. The gyrotron parts, except for the MIG, were assembled for the first bakeout. This is to avoid contamination of the MIG cathode (Fig. 10A) in the case of unforeseen failures of joints, which can lead to high pressure events during bakeout. All bolts used for assembly were lightly coated with Loctite metal-free lubricant to avoid seizing after thermocycles. A custom-built support kept the gyrotron in place during the assembly and bakeout (Fig. 10).

3.2.3. Nitrogen backfill

A nitrogen backfill was conducted to further remove any contaminants adsorbed onto the inner surface of gyrotron. According to Le Châtelier's principle, and the 2nd law of Thermodynamics, molecules adsorbed onto the surface will enter the gaseous phase when the partial pressure of that molecule decreases, until a new equilibrium is reached. The pressure of backfilling nitrogen inside the gyrotron was kept below 2 atm to prevent damage on the sapphire window.

3.2.4. Bakeout

During the bakeout, the gyrotron was heated by heating tape while the turbomolecular pump was pulling a vacuum. The heating tape was controlled by variable AC transformers (VARIAC Inc., Cleveland, OH), and monitored by thermocouples (Fig. 10B). After a uniform temperature was achieved over the gyrotron, aluminum foil was wrapped around the gyrotron for insulation (Fig. 10C). The gyrotron body was heated to 250 °C, and the collector to a higher temperature (300 °C) due to its high outgassing possibility when the spent electron beam reaches the inner surface. The bolts were tightened again at the maximum temperature due to the different expansion of copper gaskets and stainless steel. When the turbomolecular pump reported a stable pressure, the ion pumps were turned on to further pull a high vacuum. The gyrotron was slowly cooled back to room temperature once the desired pressure, $\leq 10^{-8}$ Torr, was achieved. The turbomolecular pump was connected to the arm of the gyrotron rather than to the top of the collector for Scott et al. gyrotron (Fig. 4A and B) [43], allowing a maximized cross-sectional area of the vacuum path to improve conductance.

Fig. 10. Gyrotron bakeout. (A) Assembled gyrotron connecting to a turbomolecular pump. (B) Gyrotron wrapped with heating tapes. Thermocouples are placed in different regions to monitor temperatures. (C) The gyrotron is further wrapped in aluminum foil to trap heat.

3.2.5. Activation of MIG

MIG activation involves heating the cathode with an alternating current and applying a low potential to obtain electron emission. Fig. 11A and C shows the setup for MIG activation, during which the vacuum inside MIG was maintained below 10^{-8} Torr. A circuit diagram of MIG activation is shown in Fig. 11B. The AC current was regulated by a variable transformer with a step-down converter to reduce the maximum potential. The DC potential was supplied by a Tektronix power supply (Beaverton, OR), with emission current detected by a Tektronix multimeter. The MIG was kept at a low DC potential while the cathode was hot (AC ~ 2.0 A), until an increasing emission was observed. Then the potential was slowly increased and stayed at ~15 V until the first stage of the bakeout was completed.

3.2.6. Second bakeout with MIG installed on gyrotron

All copper gaskets and bolts on the gyrotron were replaced following the first bakeout, since the copper can be deformed after compression and bolts can weaken with thermocycling. In order to avoid contamination, a nitrogen backfill was implemented during the gyrotron reassembly. The second bakeout procedure was the same as the first, except the activated MIG was attached to the vacuum tube. Heated by its internal heater with ~2.0 A alternating current, the MIG needs no heating tape on the outside. When the desired vacuum was achieved, other parts of the gyrotron were cooled gradually before the AC power in the MIG was reduced, in order to avoid gas adsorption into the porous barium-tungsten emitter.

4. Conclusion and outlook

Frequency-chirped DNP MAS achieves 19% greater DNP enhancement compared to CW irradiation, using the frequency-agile gyrotron presented here. Improvements in the interaction cavity and internal mode convertor of the gyrotron resulted in efficient microwave generation and mode conversion, thus achieving a ~3-fold gain in microwave power output compared to a previously reported gyrotron [43].

The development of a MAS microwave resonator [49] with a high quality factor would further increase electron Rabi frequencies and better manipulate electron spins. Moreover, frequency-chirped DNP MAS can be optimized in terms of the voltage waveform, rotor rotation frequency, and the type and concentration of the doped radicals. Although the microwave output was frequency-chirped, the sample was still exposed to constant high-power microwave irradiation, restraining the experimental temperatures to <100 K. However, by controlling the anode potential to terminate microwave power, frequency chirps could be performed in a way that limits the duty cycle. These methodological improvements will be necessary to perform frequency-chirped

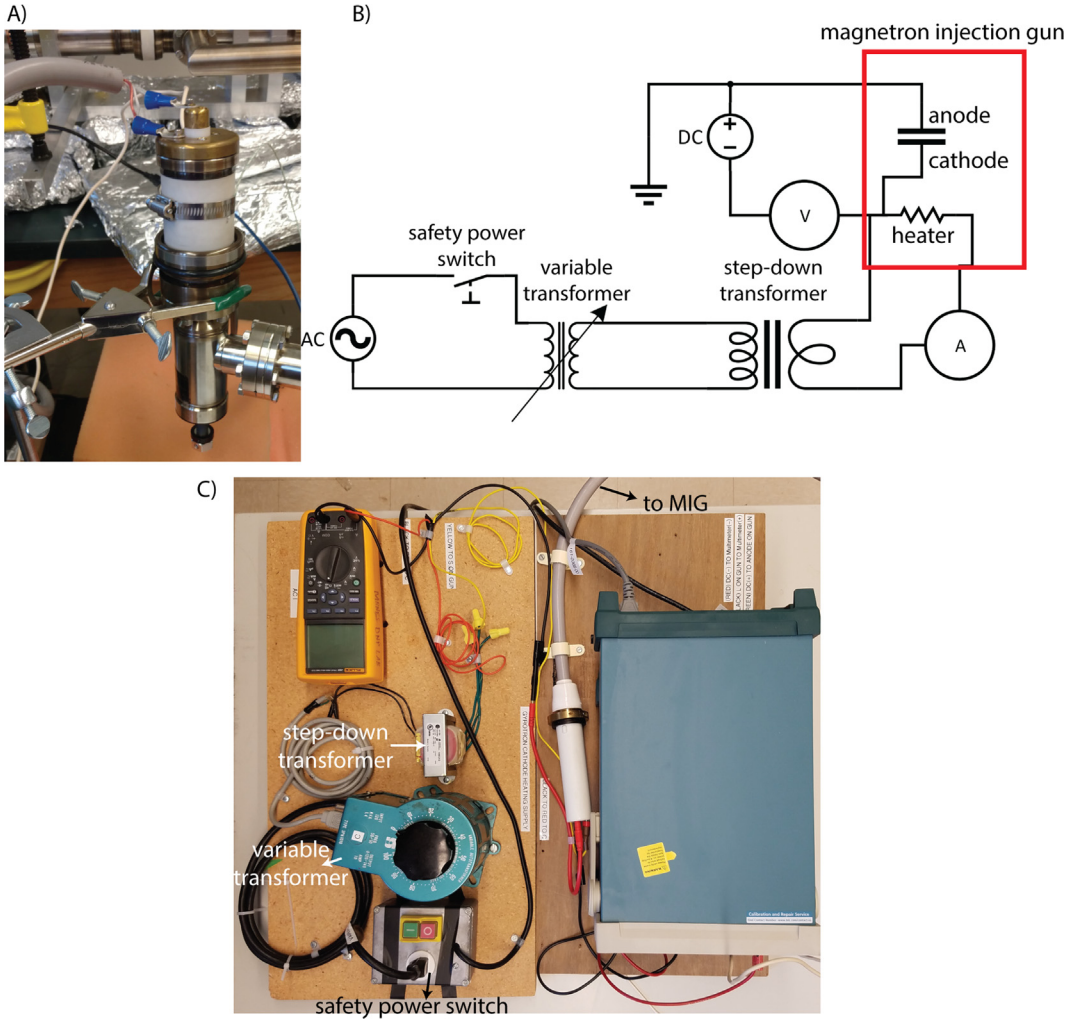

Fig. 11. MIG activation. (A) Photograph of MIG during activation. (B) Circuit diagram of the AC and DC circuits during MIG activation. (C) Photograph of the circuit diagram.

and time-domain DNP MAS at room temperature and high magnetic fields. Lastly, control over the microwave phase also holds considerable promise to improve chirped MAS-DNP, as has been discussed by the elegant unpublished work of Han and colleagues [50].

Acknowledgements

This research was supported by a NIH Director's New Innovator Award [grant number DP2GM119131], an NSF CAREER Award [grant number DBI-1553577], a Camille Dreyfus teacher-scholar award, and the Deutsche Forschungsgemeinschaft (DFG) postdoc fellowship (414196920), and the University of Iceland Research Fund.

Appendix A. Supplementary material

Supplementary data to this article can be found online at https://doi.org/10.1016/j.jmr.2019.106586.

References

[1] A.W. Overhauser, Polarization of nuclei in metals, Phys. Rev. 92 (1953) 411–415.
[2] T.R. Carver, C.P. Slichter, Polarization of nuclear spins in metals, Phys. Rev. 92 (1953) 212–213, https://doi.org/10.1103/PhysRev. 92.212.2.
[3] T. Kobayashi, A. Perras, I.I. Slowing, A.D. Sadow, M. Pruski, Dynamic nuclear polarization solid-state NMR in heterogeneous catalysis research, ACS Catal. 5 (2015) 7055–7062, https://doi.org/10.1021/acscatal.5b02039.
[4] D. Yoon, M. Soundararajan, C. Caspers, F. Braunmueller, J. Genoud, S. Alberti, J. Ansermet, 500-fold enhancement of in situ 13 C liquid state NMR using gyrotron-driven temperature-jump DNP, J. Magn. Reson. 270 (2016) 142–146, https://doi.org/10.1016/j.jmr.2016.07.014.
[5] A.S. Lilly Thankamony, J.J. Wittmann, M. Kaushik, B. Corzilius, Dynamic nuclear polarization for sensitivity enhancement in modern solid-state NMR, Prog. Nucl. Magn. Reson. Spectrosc. 102–103 (2017) 120–195, https://doi.org/10.1016/j.pnmrs.2017.06.002.
[6] M. Afeworki, J. Schaefer, Mechanism of DNP-enhanced polarization transfer across the interface of polycarbonate/polystyrene heterogeneous blends, Macromolecules 25 (1992) 4092–4096, https://doi.org/10.1021/ma00042a007.
[7] M. Afeworki, S. Vega, J. Schaefer, Direct electron-to-carbon polarization transfer in homogeneously doped polycarbonates, Macromolecules 25 (1992) 4100–4105, https://doi.org/10.1021/ma00042a009.
[8] M.J. Duijvestijn, C. van der Lugt, J. Smidt, R.A. Wind, K.W. Zilm, D.C. Staplin, 13C NMR spectroscopy in diamonds using dynamic nuclear polarization, Chem. Phys. Lett. 102 (1983) 25–28, https://doi.org/10.1016/0009-2614(83)80650-2.
[9] M.J. Duijvestijn, A. Manenschijn, J. Smidt, R.A. Wind, Structural information of undoped trans-polyacetylene obtained by 13C 2D NMR combined with dynamic nuclear polarization, J. Magn. Reson. 64 (1985) 461–469, https://doi.org/10.1016/0022-2364(85)90109-X.
[10] M. Nechtschein, F. Devreux, R.L. Greene, T.C. Clarke, G.B. Street, One-dimensional spin diffusion in polyacetylene, (CH)x, Phys. Rev. Lett. 44 (1980) 356–359, https://doi.org/10.1103/PhysRevLett. 44.356.
[11] M. Nechtschein, F. Devreux, F. Genoud, M. Guglielmi, K. Holczer, Magnetic-resonance studies in undoped trans-polyacetylene (CH)x II, Phys. Rev. B. 27 (1983) 61–78, https://doi.org/10.1103/PhysRevB.27.61.
[12] L.R. Becerra, G.J. Gerfen, R.J. Temkin, D.J. Singel, R.G. Griffin, Dynamic nuclear polarization with a cyclotron resonance maser at 5 T, Phys. Rev. Lett. 71 (1993) 3561–3564, https://doi.org/10.1103/PhysRevLett. 71.3561.
[13] K.-N. Hu, H. Yu, T.M. Swager, R.G. Griffin, Dynamic nuclear polarization with biradicals, J. Am. Chem. Soc. 126 (2004) 10844–10845, https://doi.org/10.1021/ja039749a.
[14] V.S. Bajaj, M.L. Mak-Jurkauskas, M. Belenky, J. Herzfeld, R.G. Griffin, Functional and shunt states of bacteriorhodopsin resolved by 250 GHz dynamic nuclear polarization-enhanced solid-state NMR, Proc. Natl. Acad. Sci. 106 (2009) 9244–9249, https://doi.org/10.1073/pnas.0900908106.
[15] X. Kang, A. Kirui, A. Muszyński, M.C.D. Widanage, A. Chen, P. Azadi, P. Wang, F. Mentink-Vigier, T. Wang, Molecular architecture of fungal cell walls revealed by solid-state NMR, Nat. Commun. 9 (2018) 1–12, https://doi.org/10.1038/s41467-018-05199-0.
[16] X. Kang, A. Kirui, M.C. Dickwella Widanage, F. Mentink-Vigier, D.J. Cosgrove, T. Wang, Lignin-polysaccharide interactions in plant secondary cell walls revealed by solid-state NMR, Nat. Commun. 10 (2019) 1–9, https://doi.org/10.1038/s41467-018-08252-0.
[17] R.W. Martin, R.C. Jachmann, D. Sakellariou, U.G. Nielsen, A. Pines, High-resolution nuclear magnetic resonance spectroscopy of biological tissues using projected angle spinning, Magn. Reson. Med. 257 (2005) 253–257, https://doi.org/10.1002/mrm.20585.
[18] A.N. Smith, U.T. Twahir, T. Dubroca, G.E. Fanucci, J.R. Long, N. High, M. Field, E. P. Dirac, U. States, Molecular rationale for improved dynamic nuclear polarization of biomembranes, J. Phys. Chem. B. 120 (2016) 7880–7888, https://doi.org/10.1021/acs.jpcb.6b02885.
[19] W. Tang, A. Bhatt, A.N. Smith, P.J. Crowley, L.J. Brady, J.R. Long, Specific binding of a naturally occurring amyloidogenic fragment of *Streptococcus mutans* adhesin P1 to intact P1 on the cell surface characterized by solid state NMR spectroscopy, J. Biomol. NMR 64 (2016) 153–164, https://doi.org/10.1007/s10858-016-0017-1.
[20] D. Daube, M. Vogel, B. Suess, B. Corzilius, Dynamic nuclear polarization on a hybridized hammerhead ribozyme: an explorative study of RNA folding and direct DNP with a paramagnetic metal ion cofactor, Solid State Nucl. Magn. Reson. 101 (2019) 21–30, https://doi.org/10.1016/j.ssnmr.2019.04.005.
[21] T.V. Can, J.J. Walish, T.M. Swager, R.G. Griffin, Time domain DNP with the NOVEL sequence, J. Chem. Phys. 143 (2015) 1–8, https://doi.org/10.1063/1.4927087.
[22] A. Henstra, P. Dirksen, W.T. Wenckebach, Enhanced dynamic nuclear polarization by the integrated solid effect, Phys. Lett. A. 134 (1988) 134–136, https://doi.org/10.1016/0375-9601(88)90950-4.
[23] T.V. Can, R.T. Weber, J.J. Walish, T.M. Swager, R.G. Griffin, Frequency-swept integrated solid effect, Angew. Chemie – Int. Ed. 56 (2017) 6744–6748, https://doi.org/10.1002/anie.201700032.
[24] A. Henstra, P. Ducksen, J. Schmidt, K. Onnes, H. Laboratories, Nuclear spin orientation via electron spin locking (NOVEL), J. Magn. Reson. 393 (1988) 389–393.
[25] I. Kaminker, S. Han, Amplification of dynamic nuclear polarization at 200 GHz by arbitrary pulse shaping of the electron spin saturation profile, J. Phys. Chem. Lett. 9 (2018) 3110–3115, https://doi.org/10.1021/acs.jpclett.8b01413.
[26] D. Yoon, M. Soundararajan, P. Cuanillon, F. Braunmueller, S. Alberti, J.P. Ansermet, Dynamic nuclear polarization by frequency modulation of a tunable gyrotron of 260 GHz, J. Magn. Reson. 262 (2016) 62–67, https://doi.org/10.1016/j.jmr.2015.11.008.
[27] A. Bornet, A. Pinon, A. Jhajharia, M. Baudin, X. Ji, L. Emsley, G. Bodenhausen, J.H. Ardenkjaer-Larsende, S. Jannin, Microwave-gated dynamic nuclear polarization †, Phys. Chem. Chem. Phys. (2016) 30530–30535, https://doi.org/10.1039/c6cp05587g.
[28] S. Alberti, J.P. Ansermet, K.A. Avramides, D. Fasel, J.P. Hogge, S. Kern, C. Lievin, Y. Liu, A. Macor, I. Pagonakis, M. Silva, M.Q. Tran, T.M. Tran, D. Wagner, Design of a frequency-tunable gyrotron for DNP-enhanced NMR spectroscopy, in: 34th Int. Conf. Infrared, Millimeter, Terahertz Waves, IRMMW-THz 2009. (2009) 1–2. doi: 10.1109/ICIMW.2009.5324906.
[29] V. Vitzthum, M.A. Caporini, G. Bodenhausen, Solid-state nitrogen-14 nuclear magnetic resonance enhanced by dynamic nuclear polarization using a gyrotron, J. Magn. Reson. 205 (2010) 177–179, https://doi.org/10.1016/j.jmr.2010.04.014.
[30] M.Y. Glyavin, A.V. Chirkov, G.G. Denisov, A.P. Fokin, V.V. Kholoptsev, A.N. Kuftin, A.G. Luchinin, G.Y. Golubyatnikov, V.I. Malygin, M.V. Morozkin, V.N. Manuilov, M.D. Proyavin, A.S. Sedov, E.V. Sokolov, E.M. Tai, A.I. Tsvetkov, V.E. Zapevalov, Experimental tests of a 263 GHz gyrotron for spectroscopic applications and diagnostics of various media, Rev. Sci. Instrum. 86 (2015) 1–4, https://doi.org/10.1063/1.4921322.
[31] A.C. Torrezan, S.T. Han, I. Mastovsky, M.A. Shapiro, J.R. Sirigiri, R.J. Temkin, A.B. Barnes, R.G. Griffin, Continuous-wave operation of a frequency-tunable 460-GHz second-harmonic gyrotron for enhanced nuclear magnetic resonance, IEEE Trans. Plasma Sci. 38 (2010) 1150–1159, https://doi.org/10.1109/TPS.2010.2046617.
[32] S. Alberti, F. Braunmueller, T.M. Tran, J. Genoud, J. Hogge, M.Q. Tran, J. Ansermet, Nanosecond pulses in a THz gyrotron oscillator operating in a mode-locked self-consistent Q-switch regime, Phys. Rev. Lett. 205101 (2013) 1–5, https://doi.org/10.1103/PhysRevLett. 111.205101.
[33] Y. Matsuki, H. Takahashi, K. Ueda, T. Idehara, I. Ogawa, M. Toda, H. Akutsu, T. Fujiwara, Dynamic nuclear polarization experiments at 14.1 T for solid-state NMR, Phys. Chem. Chem. Phys. 12 (2010) 5799–5803.
[34] Y. Matsuki, T. Idehara, J. Fukazawa, T. Fujiwara, Advanced instrumentation for DNP-enhanced MAS NMR for higher magnetic fields and lower temperatures, J. Magn. Reson. 264 (2016) 107–115, https://doi.org/10.1016/j.jmr.2016.01.022.
[35] K. Ueda, Y. Matsuki, T. Fujiwara, Y. Tatematsu, I. Ogawa, T. Idehara, Further characterization of 394-GHz Gyrotron FU CW GII with additional PID control system for 600-MHz DNP-SSNMR spectroscopy, J. Infrared Millimeter Terahertz Waves (2016) 825–836, https://doi.org/10.1007/s10762-016-0276-7.
[36] M. Blank, P. Borchard, S. Cauffman, K. Felch, M. Rosay, L. Tometich, High-frequency CW Gyrotrons for NMR/DNP applications, IVEC 2012 (2012) 327–328, https://doi.org/10.1109/IVEC.2012.6262182.
[37] D.J. Singel, H. Seidel, R.D. Kendrick, C.S. Yannoni, A spectrometer for EPR, DNP, and multinuclear high-resolution NMR, J. Magn. Reson. 81 (1989) 145–161, https://doi.org/10.1016/0022-2364(89)90273-4.
[38] R.A. Wind, R.A. Hall, A. Jurkiewicz, H. Lock, G.E. Maciel, Two novel DNP-NMR probes, J. Magn. Reson. Ser. A. 110 (1994) 33–37, https://doi.org/10.1006/jmra.1994.1177.
[39] G. Mathies, M.A. Caporini, V.K. Michaelis, Y. Liu, K. Hu, D. Mance, J.L. Zweier, M. Rosay, M. Baldus, R.G. Griffin, Efficient dynamic nuclear polarization at 800 MHz/527 GHz with trityl-nitroxide biradicals, Angew. Chem - Int. Ed. 54 (2015) 11770–11774, https://doi.org/10.1002/anie.201504292.

[40] Y. Liu, F.A. Villamena, J.L. Zweier, Trityl-nitroxide biradicals as unique molecular probes for the simultaneous measurement of redox status and oxygenation, Chem. Commun. 1 (2010) 628–630, https://doi.org/10.1039/b919279d.
[41] E.P. Saliba, E.L. Sesti, F.J. Scott, B.J. Albert, E.J. Choi, N. Alaniva, C. Gao, A.B. Barnes, Electron decoupling with dynamic nuclear polarization in rotating solids, J. Am. Chem. Soc. 139 (2017) 6310–6313, https://doi.org/10.1021/jacs.7b02714.
[42] E.L. Sesti, E.P. Saliba, N. Alaniva, A.B. Barnes, Electron decoupling with cross polarization and dynamic nuclear polarization below 6 K, J. Magn. Reson. 295 (2018) 1–5, https://doi.org/10.1016/j.jmr.2018.07.016.
[43] F.J. Scott, E.P. Saliba, B.J. Albert, N. Alaniva, E.L. Sesti, C. Gao, N.C. Golota, E.J. Choi, A.P. Jagtap, J.J. Wittmann, M. Eckardt, W. Harneit, B. Corzilius, S.Th. Sigurdsson, A.B. Barnes, Frequency-agile gyrotron for electron decoupling and pulsed dynamic nuclear polarization, J. Magn. Reson. 289 (2018) 45–54, https://doi.org/10.1016/j.jmr.2018.02.010.
[44] A.E. Bennett, C.M. Rienstra, M. Auger, K.V. Lakshmi, R.G. Griffin, Heteronuclear decoupling in rotating solids, J. Chem. Phys. 103 (1995) 6951–6958, https://doi.org/10.1063/1.470372.
[45] K.R. Thurber, R. Tycko, Measurement of sample temperatures under magic-angle spinning from the chemical shift and spin-lattice relaxation rate of 79 Br in KBr powder, J. Magn. Reson. 196 (2009) 84–87, https://doi.org/10.1016/j.jmr.2008.09.019.
[46] CPI, CGY-8026 Gyrotron Oscillator; 2012. p. 1–2.
[47] A.B. Barnes, E.A. Nanni, J. Herzfeld, R.G. Griffin, R.J. Temkin, A 250 GHz gyrotron with a 3 GHz tuning bandwidth for dynamic nuclear polarization, J. Magn. Reson. 221 (2012) 147–153, https://doi.org/10.1016/j.jmr.2012.03.014.
[48] F.J. Scott, N. Alaniva, N.C. Golota, E.L. Sesti, E.P. Saliba, L.E. Price, B.J. Albert, P. Chen, R.D. O'Connor, A.B. Barnes, A versatile custom cryostat for dynamic nuclear polarization supports multiple cryogenic magic angle spinning transmission line probes, J. Magn. Reson. 297 (2018) 23–32, https://doi.org/10.1016/J.JMR.2018.10.002.
[49] F.J. Scott, E.L. Sesti, E.J. Choi, A.J. Laut, J.R. Sirigiri, A.B. Barnes, Magic angle spinning NMR with metallized rotors as cylindrical microwave resonators, Magn. Reson. Chem. 56 (2018) 831–835, https://doi.org/10.1002/mrc.4744.
[50] A. Equbal, K. Tagami, S. Han, Rotor-synchronous Non-CW DNP Under Magic-Angle Spinning, Experimental NMR Conference. (2019).